A Low-Complexity 6DOF Magnetic Tracking System Based on Pre-Computed Data Sets for Wearable Applications

A Low-Complexity 6DOF Magnetic Tracking System Based on Pre-Computed Data Sets for Wearable Applications

David A. Fernandez G.[†‡], Paolo Motto Ros[‡], Danilo Demarchi[‡] and Marco Crepaldi[†]
[†] = Electronic Design Laboratory (EDL), Istituto Italiano di Tecnologia.
[‡] = Department of Electronics and Telecommunications, Politecnico di Torino.

***Abstract*—We present a 6DOF magnetic tracking system based on a low-complexity algorithm, operating with an Inertial Measurement Unit (IMU) orientation estimation and regression functions formed with simulated data sets, capable of running using only a single microcontroller unit (MCU), for use in low-complexity wearable and wireless systems. A prototype based on a commercial magnetometer and IMU, a Cortex-M4 MCU was implemented and tested in both static and dynamic conditions, using a VICON motion tracking system as reference. Static and dynamic spatial accuracy performance is 2.6 mm and 5.4 mm respectively, after applying a calibration procedure based on a two layers Neural Network (NN) and a measured data set. Comparison with the state-of-the-art, supported by a defined Figure-of-Merit (FoM) show excellent performance compared to commercial and research systems in a low-complexity and portable solution.**

***Index Terms*—6DOF, Magnetic tracking, High accuracy, Low complexity, Wireless ready.**

I. Introduction

THE accurate tracking of objects inside a determined space has been recently identified of great interest in various research fields. The necessity of immersive human-machine interaction have been manifested in the entertainment industry [1], medical instrumentation development [2], neuroscience research [3] and sport engineering [4]. Being able to comprehend and quantize how the human joints move or an inanimate object is manipulated with a minimum required accuracy is the key to open the door to endless interactive applications. The application domains range from entertainment systems such as Microsoft Kinect® [5], which requires the position estimation of several points with centimeter-level accuracy inside a single room, to image-guided surgical instrumentation [6] which requires the position estimation of few points with submillimeter-level accuracy inside a few centimeters range. The technology and techniques implemented for positioning systems varies accordingly to their specific application.

Tracking systems can be divided into three categories based on their applications requirements in terms of range and accuracy. The first of these categories are the global tracking systems, such as GPS, Galileo and GLONASS, that allow the localization of a device in an open field around globe with an accuracy of few meters. Next, site-wide tracking systems can be considered. They allow the localization of a device inside and within the range of a building with an accuracy below one meter. For this purpose different radio frequency systems such as Ultra-Wideband (UWB) systems [7], [8], Radio Frequency Identification (RFID) [9], Wi-Fi hotspots [10] and Bluetooth 5.1 beacons arrays [11], [12] can be used with variable techniques such as Time of Arrival (TOF), Time Difference of Arrival (TDOF), Angle of Arrival (AOA) or Angle of Departure (AOD). Then workspace tracking systems can be considered as the final category. These allow the localization of devices inside a space limited to few cubic meters with a centimeter and even millimeter-level accuracy. Due to these characteristics, most immersive interactive applications can be developed with workspace tracking systems. Several techniques and technologies can be used to achieve these type of system performances, however, optical and magnetic tracking are so far the only applicable solutions to reach millimeter-level accuracy and below.

Optical tracking systems range from devices that perform below millimeter-level tracking of retro-reflective markers inside a range of few meters such as VICON® [13] and NDI optical systems [14], to devices that provides millimeter-level accuracy tracking the human fingers inside a few centimeter range such as Leap Motion® [15], [16]. Magnetic tracking systems either commercially available such as Razer Hydra® [17], Polhemus [18], [19], [20] and NDI magnetic systems [14] or research prototypes such as Finexus [21] and IM6D [22], are able to track objects with a millimeter-level accuracy and below within lower ranges than most considered optical tracking systems. Comparing both optical and magnetic solutions, it can be found that the main differences between them are the working range, which is usually larger for optical systems, and the requirement of a Line-Of-Sight (LOS) or the challenge to operate without it [23]. Optical tracking systems can not work without a LOS between the tracked object and the system, while magnetic systems are independent as long as the tracking space is clear from ferromagnetic materials. In order to counteract this dependency, optical systems require the use of multiple stereo-cameras, as a mean to maintain the LOS with at least one camera. Moreover, since the cameras need to be installed in fixed and calibrated positions to keep the tracking space reference, this makes magnetic systems a more portable and flexible solution. However, one weak point of current magnetic tracking systems is the lack of a wireless connectivity, since most systems have the tracked device wired

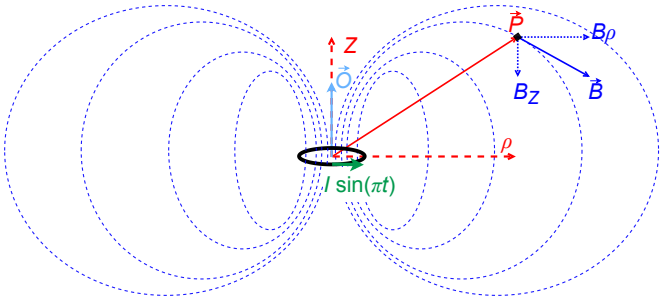

Fig. 1: Magnetic flux density lines of a magnetic dipole created by a current loop around the Z axis.

to its processing unit, which might limit the mobility of human joints when been worn, limiting therefore their use in immersive human-machine interactive applications, in comparison to optical tracking systems. Applications such as [24], [25], [26] could be enhanced by replacing the reported tablet-based systems with a 3D millimeter-accurate tracking system with non-LOS performance dependence, hence allowing further explorations of human-machine interfaces (HMI) for visually impaired users. Moreover, [27] shows other HMI applications examples based on wearable magnetic tracking systems. The immersiveness of such applications could be enhanced by the introduction of 6DOF and multiple sensor tracking.

This paper proposes a magnetic tracking system based on a simplified position and orientation estimation algorithm suitable for use in wearable devices with wireless interfacing by establishing low power and data rate throughput limits. Prior to the system usage, a simulation of the generated magnetic field is calculated on a large number of different position points. Then a scattered interpolation is formed to build the magnetic sensor position as a function of the measured magnetic flux, in order to reduce its estimation computational time. The system uses a high-speed digital magnetic sensor to capture the generated field, paired with an Inertial Measurement Unit (IMU) to estimate its orientation through sensor data fusion. This concept enables the deployment of low-cost embedded 6 Degrees Of Freedom (6DOF) magnetic tracking systems. This paper is a continuation of what was presented in [28] and it is organized as follows. Sec. II introduces the magnetic tracking system concept and Sec. III presents the associated required low-complexity hardware. Sec. IV presents in detail the tracking algorithm implementation while a proof-of-concept implementation is discussed and validated in Sec. V. Sec. VII concludes the paper.

II. Magnetic Tracking System

Magnetic tracking is based on the exploitation of the dependency of a measurement taken by a magnetic flux density $\vec{B}$ sensor on its position $\vec{P}$ and orientation $\vec{O}$ with respect to the field generator. This dependency can be expressed as a mathematical model of the magnetic field. Such model performance heavily depends on the environment composition, the field generator geometry and materials, and could be solved through Maxwell's equations. In order to simplify the presented problem, the model of a magnetic dipole in vacuum

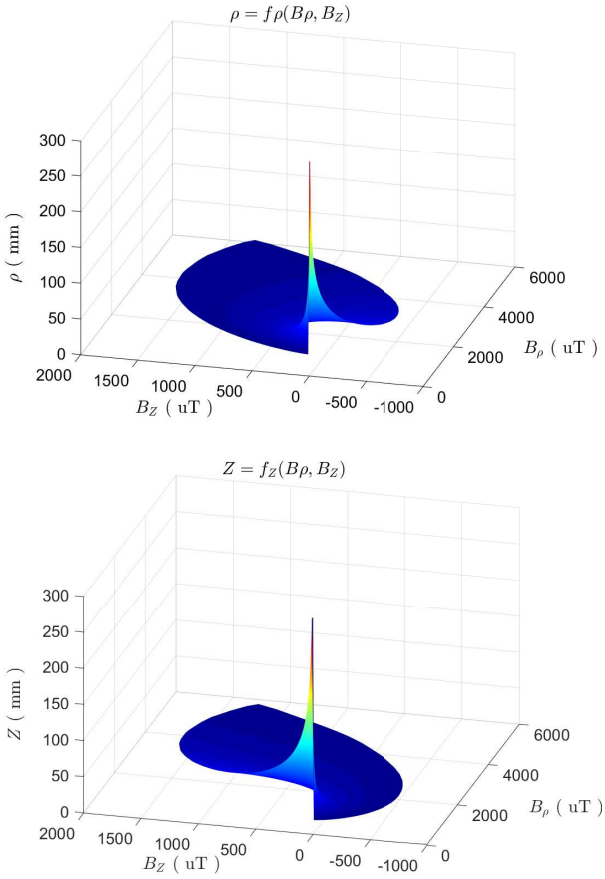

Fig. 2: Sensor coordinates ρ (a) and Z (b) as a function of magnetic flux measurements B_ρ and B_Z.

can be considered, then, as observed in Fig. 1, the magnetic flux density $\vec{B}$ measured in the point $\vec{P}$ can be expressed as (see [29]),

$$\vec{B} = \frac{\mu_0 M_T}{4\pi}\left(\frac{3\left(\vec{O}\cdot\vec{P}\right)\vec{P}}{R^5} - \frac{\vec{O}}{R^3}\right) \tag{1}$$

where $M_T = NI$ is the magnetic dipole moment with N the current loop turns number and I the current magnitude, $R = \|\vec{P}\|$ with $\vec{P}$ the magnetic sensor position, $\vec{O}$ is the unit vector oriented with the north pole of the magnetic dipole, and μ_0 is the vacuum permittivity. Even if the above model can not accurately describe the field generated by a bobbin coil, it remains valid for certain implementations assuming the sensor to bobbin distance greater than four times the current loop radius [30]. A more accurate representation of the field generated by an air bobbin coil, solved through elliptic integrals can be found in [31]. However, this model cannot be correctly applied when a high permeability material is used as the bobbin core to increase the generated field magnitude, due to the permeability non-linearity.

In order to calculate $\vec{B} = f(\vec{P}, \vec{O})$ for more complex structures such as the bobbin coil with ferromagnetic core, Finite Element Methods (FEM) modeling can be used to solve numerically the correspondent Maxwell's equations. However, the objective is to estimate the sensor position using magnetic

flux density measurements, therefore a way to perform the inverse function $\vec{P} = f_P(\vec{B}, \vec{O})$ is needed. It can be seen from the simplest magnetic flux model represented in Eq. (1), that performing the regression estimation is not an simple task. One commonly used tool to solve this regression problem is the non-linear least squares method. However, this requires a high computational power for a real-time application with a high update rate, and leads to a not anymore wearable processing hardware, therefore limiting the capability of a magnetic tracking system to be designed as a wearable device in comparison to optical tracking systems. As a possible solution, we propose partitioning our tracking space of interest and form a regular grid of numerous position points $\{\vec{P}_i\}$, then from a FEM model of the magnetic flux density $\vec{B}$ extract $\{\vec{B}_i\} = f(\{\vec{P}_i\})$ for each one of these points and finally, using the scattered interpolation method, form the regressions functions $\vec{P} = f_P(\vec{B})$, as shown in [28]. A similar regression method is exposed in [32], where a look-up table is used to pair known positions points $\{\vec{P}_i\}$ with their correspondent magnetic flux density $\{\vec{B}_i\}$ or voltage measurement. Such method would also allow a fast real-time computation however, the trade-off of needing more memory space depending the required accuracy and range, needs to be taken into account for resource constrained wearable devices. Fig. 2 shows a graphical representation of the regression functions, defined here as,

$$\vec{P} = [\rho,\ Z] = [f_\rho(B_\rho, B_Z), f_Z(B_\rho, B_Z)] \tag{2}$$

formed with a 2D FEM model of a bobbin coil, using a set of points $\vec{P}$, from $\rho = 2\,\text{cm}$ to $\rho = 30\,\text{cm}$, and $Z = 2\,\text{cm}$ to $Z = 30\,\text{cm}$, with $1\,\text{mm}$ spacing between points. Taking into account the axial symmetry of the field generated by a current loop as shown in Fig. 1, the problem can be simplified to a two dimensional (2D) model dependent on the coordinates ρ and Z. To use this 2D solution for a three-dimensional (3D) problem, some assumptions and limitations need to be taken into account. Firstly, to ensure a single pair of magnetic flux density B_ρ and B_Z, for every point $\vec{P}_i$, it is necessary to work in the space $Z \geq 0$. Then, as showed in Fig. 3, using a tri-axial magnetic flux density sensor, the 3D problem can be solved according to the following steps:

1) Sense the magnetic flux density in the sensor position as B_X, B_Y and B_Z;
2) Calculate $B_\rho = \sqrt{B_{X'}^2 + B_{Y'}^2}$;
3) Estimate ρ and Z from the regression functions Eq. (2), while θ is the B_ρ projection angle in the $X'Y'$ plane.

This solution, however, is only applicable when the sensor axes $[X',\ Y',\ Z']$ and the system axes $[X,\ Y,\ Z]$ are aligned, therefore the sensor measurements $B_{X'}$, $B_{Y'}$ and $B_{Z'}$ correspond to their system referenced components B_X, B_Y and B_Z. Observe that when the sensor and system axes are misaligned, the relative sensor orientation with respect to the system axes needs to be known. This relative orientation can be determined using IMU sensors, which are composed by accelerometer, gyroscope and low sampling rate magnetic sensors through the use of available Attitude Heading Reference System (AHRS) algorithms. For this purpose we considered the Madgwick's algorithm [33]. It is an open source AHRS algorithm, characterized by a low computational cost. In [33], [34] the algorithm is compared to Kalman Filter (KF) based AHRS algorithms, showing similar accuracy without the use of computationally expensive matrix inversion required by a KF. Moreover, [34], [35] show that the algorithm can be easily integrated in dead reckoning position systems and to enhance their performances. Furthermore, [36] experimentally compares Madgwick's algorithm with an Extended Kalman Filter (EKF) based AHRS running on a M4-Cortex microcontroller, getting slightly better accuracy results using the EKF at the expense of a computational cost one order of magnitude higher. We have then chosen Madgwick's algorithm to estimate both sensor and system orientation with respect to the Earth in form of quaternions $q = e^{\frac{\alpha}{2}(u_X\hat{\imath}+u_Y\hat{\jmath}+u_Z\hat{k})} = \cos(\frac{\alpha}{2}) + \sin(\frac{\alpha}{2})(u_X\hat{\imath}+u_Y\hat{\jmath}+u_Z\hat{k})$. The quaternions represent a rotation of α around the unit vector $u_X\hat{\imath}+u_Y\hat{\jmath}+u_Z\hat{k}$. Having both the sensor and system earth referenced quaternions, q_S and q_0 respectively, the relative sensor orientation with respect to the system can be calculated as the Hamilton product as follow,

$$q_R = q_S \times q_0^{-1}. \tag{3}$$

The system referenced magnetic flux measurement can now be estimated as,

$$\vec{B_R} = q_R \times \vec{B} \times q_R^{-1} = [B_X,\ B_Y,\ B_Z]. \tag{4}$$

where $\vec{B} = [B_{X'},\ B_{Y'},\ B_{Z'}]$ is the sensed magnetic flux density referred to the sensor axes $[X',\ Y',\ Z']$.

Finally, in order to avoid mixing with the Earth and power lines magnetic fields and still let the problem be considered quasi-static, a low frequency field is generated, in this particular case with frequency between 70 Hz and 1 kHz. Therefore, the sensed magnetic flux density can be considered variable in time with the following form,

$$\vec{B_R}(t) = \vec{B_R}\sin(2\pi f_0 t + \phi), \tag{5}$$

where $\vec{B_R}$ is still composed as expressed in Eq. 4. Since we intend to use the B_ρ projection angle θ in the $X'Y'$ plane

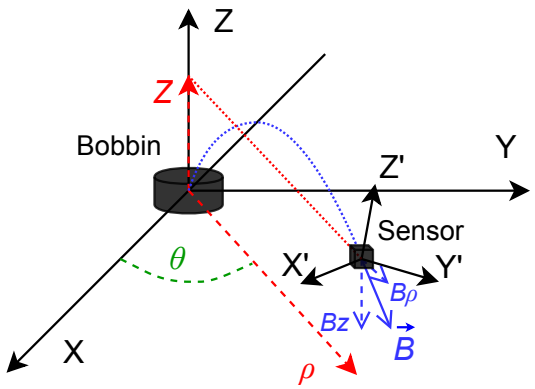

Fig. 3: Sensed magnetic flux density vector components B_ρ and B_Z, and cylindrical sensor coordinates ρ, Z and θ with respect to the system axes.

(Fig. 3), as part of the position estimation procedure, having a vector that varies over time leaves two options to apply it. On one side having a full synchronization with magnetic field generator would allow to know exactly the sensed magnetic flux density phase ϕ. Otherwise, using a tracking space limited by either $X > 0$ or $Y > 0$ would allow to be able to assume respectively $B_{X'}$ or $B_{Y'}$, as an always positive component and use this sensed signal to calculate ϕ. At this point, by knowing ϕ we can extract the sensed $\vec{B_R}(t)$ amplitude $\vec{B_R}$ with its correspondent direction and use the previously explained method to estimate the sensor position $\vec{P}$.

III. System-level Hardware Architecture

To implement the previously described technique inside a wearable device, a system-level hardware architecture is conceptualized according to the diagram shown in Fig. 4. The system is divided in two modules, the field generator module and the sensing module, interfaced to an end-user device functioning as Graphical User Interface (GUI).

The field generator module is in charge of generating the oscillating magnetic field with a low frequency. It comprises a micro-controller unit (MCU) that generates the sinusoidal signal, that is power amplified before feeding a single axial cylindrical bobbin coil. An IMU mechanically fixed to the bobbin coil is sampled by the same MCU to set the system axes orientation with respect to Earth. A Bluetooth Low Energy (BLE) module allows the wireless communication with the final user device running the GUI. Finally, a power supply unit powers both the MCU and the amplifier.

The sensing module comprises multiple couples of tri-axial magnetic flux density and IMU sensors controlled by a MCU which is also in charge of processing the sensor signals to estimate both its position and orientation with respect to the bobbin coil and the field generator IMU, respectively. To allow high-levels of wearability a rechargeable Li-Po battery-based powering system and a BLE module can be used for wireless communication in order to send the tracked sensors processed data to the GUI. As mentioned in Sec. II, it is important to take into account that if the regression functions in Eq. (2) are implemented inside the sensing module MCU, it is necessary to trade-off between the regressions function accuracy and range, and the required Random Access Memory (RAM) space from the MCU. This trade-off will be further discussed in Sec. IV as a mean to set the required MCU RAM size.

Finally, the GUI will run in the end-user device connected to both modules via BLE allowing the field generator module control and receiving the sensor module data. As an alternative solution, the GUI could run the regression functions Eq. (2) if the application requires a large accuracy and range, demanding a memory space higher than the MCU available RAM. As it will be explained in Sec. IV, low-power wireless solution is viable since the BLE required data throughput is the same before and after the regression functions use. However, we considered it of secondary importance since it depends on the final user device characteristics and not the tracking system itself, which is the core contribution.

IV. Tracking algorithm implementation

The magnetic developed tracking algorithm was designed to be run on the sensing module MCU for each sensor couple, so as to accomplish the procedure described in Sec. II with a wearable and wireless hardware designed as proposed by the system level architecture described in Sec. III. Prior to the device usage, the system axes orientation with respect to the Earth q_0 must be calculated using the field generator module IMU data and the Madgwick's algorithm. As showed in Fig. 5, a first stage of the sensing module algorithm will sample the magnetic sensor with $800\,{}^{\text{samples}}/_{\text{s}}$ and filter it with a low-pass filter with $15\,\text{Hz}$ cut-off frequency. Then, the sensed earth magnetic flux density, the IMU accelerometer and gyroscope measurements, and the previously computed system quaternion q_0 will be used inside the Madgwick's algorithm to compute the sensor couple relative quaternion q_R at $100\,{}^{\text{samples}}/_{\text{s}}$. On a second stage, the raw magnetic sensor set of 8 measurements is rotated by the conjugated quaternion q_R^{-1} and then band-pass filtered with a $30\,\text{Hz}$ bandwidth around the variable magnetic field frequency $f_0 = 100\,\text{Hz}$ as showed in Eq. (5), allowing the extraction of a single sine wave period. A third stage will extract the $\vec{B_R}$ envelope from the filtered signal $\vec{B_R}(t)$ with a $100\,{}^{\text{samples}}/_{\text{s}}$ rate. By reducing the tracking space to $Z > 0$ and $Y > 0$, B_Y component will be always considered positive and the phase between $B_Y \sin(2\pi f_0 t + \phi)$ and both $B_X \sin(2\pi f_0 t + \phi)$, $B_Z \sin(2\pi f_0 t + \phi)$, will be used to determine the sign of both B_X and B_Z. The final stage of the algorithm will transform $\vec{B_R}$ into the estimated coordinates $\vec{P} = [X, Y, Z]$. For this purpose, firstly B_ρ is calculated as the norm of B_X and B_Y, then using the regression functions described in Sec. II Eq. (2) are calculated.

In order to run these functions on an MCU, it is possible to use only a limited number of point to form the scattered interpolation of the regression functions in Eq. (2). The trade-off in this case resides in the chosen number of points to build the scattered interpolations and the consequent needed memory space and accuracy. To estimate the required memory, besides the number of point to be used, it is necessary to know the number of triangles formed with a Delaunay triangulation of such set of point. Then to solve the linear interpolation as shown in [37] the minimum required memory can be estimated as an array of $4 \times N$ for N points containing the points coordinates $[B_\rho, B_Z, \rho, Z]$, plus an array of $6 \times M$ for M triangles containing the vertex and triangle connectivity lists.

Fig. 6 shows the interpolations smoothness decrease and the error of the interpolation created with $\Delta\rho = \Delta_Z = 10\,\text{mm}$ with respect to an ideal interpolation created with a $\Delta\rho = \Delta_Z = 1\,\text{mm}$ separation grid. Tab. I compares the required memory space and root-mean-squared-error (RMSE) of each one of the scattered interpolations created using both floating point and 16-bit fixed point precision for both points and triangles information arrays, and different spacing grids with respect to the ideal interpolation created with floating point precision and a $\Delta\rho = \Delta_Z = 1\,\text{mm}$. It can be seen that using a fixed point precision introduces a negligible error in comparison to the error introduced by the use of a higher grid spacing. Alternatively, such memory limitations can be avoided if the

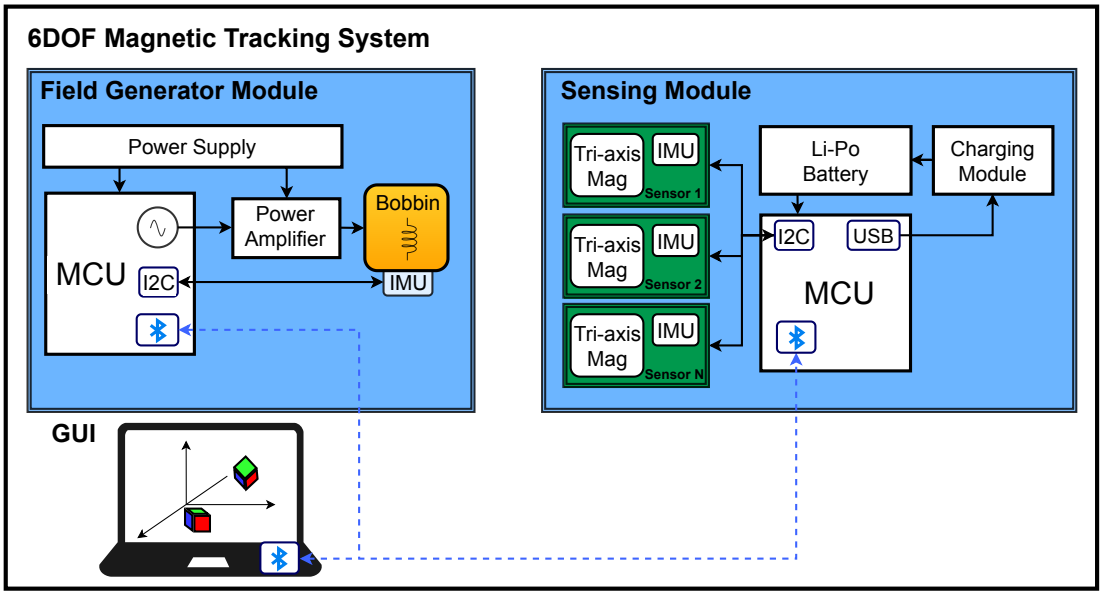

Fig. 4: System-level conceptual hardware architecture. The system is divided in two modules, the field generator module, which is in charge of generating the AC magnetic field and the sensing module, which processes the sensed signals and estimates the magnetic sensors relative position. Additionally a device connected wirelessly to the modules will contain the system graphical user interface.

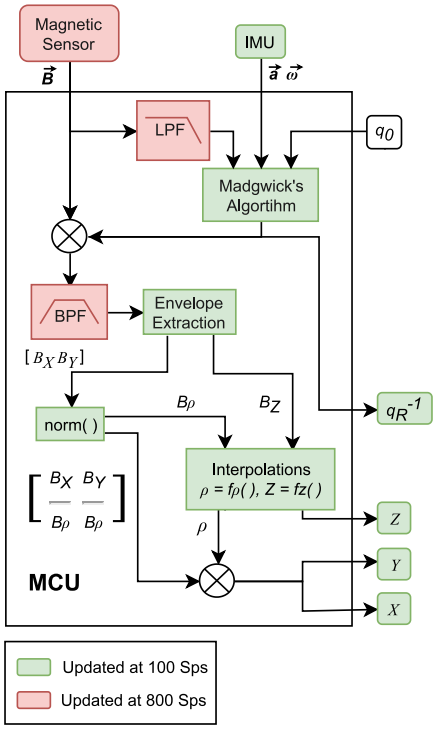

Fig. 5: Algorithm implementation flowchart to estimate position and orientation of a single tri-axial magnetic and IMU sensor couple.

scattered interpolations are implemented in the end-user device instead of the MCU, provided that it is capable of running these calculations in real time and have enough available RAM. This is possible only after the signal processing stages and not before because the necessary data throughput depends

TABLE I: Comparison of Different Scattered Interpolations of Functions $f_\rho(B_\rho, B_Z)$ and $f_Z(B_\rho, B_Z)$

Grid spacing (mm)	# points	# triangles	Precision	Memory Size (kB)	RMSE (mm)
1	302960	605876	Floating Point	24236	-
			Fixed Point	9694.2	0.0475
5	3080	6130	Floating Point	245.79	0.419
			Fixed Point	98.2	0.422
10	784	1541	Floating Point	62.189	0.8313
			Fixed Point	24.764	0.8322

on the magnetic sensor sampling rate, which in this case (see the following section) is $800\,^{\text{samples}}/_{\text{s}}$ but could be higher (when using an analogue magnetic sensor and an analogue to digital converter). In the envelope extraction block output the update rate can be controlled and adapted to a low power wireless communication data throughput.

V. Proof-of-Concept and Experimental Results

In order to verify the previously discussed methods, a laboratory system prototype was implemented. Fig. 7 shows the tracking sensor module prototype. It has been developed using the 9-axis IMU MPU9250 which is commonly used for orientation estimation applications and is composed by an accelerometer with sampling frequencies from $4\,\text{Hz}$ to $4\,\text{kHz}$, sensitivity from 2.048 to $16.38\,^{\text{LSB}}/_{\text{G}}$ and full scale ranges from ± 2 to $\pm 16\,\text{G}$. The gyroscope provides sampling frequencies from $4\,\text{Hz}$ to $4\,\text{kHz}$, sensitivities from 16.4 to

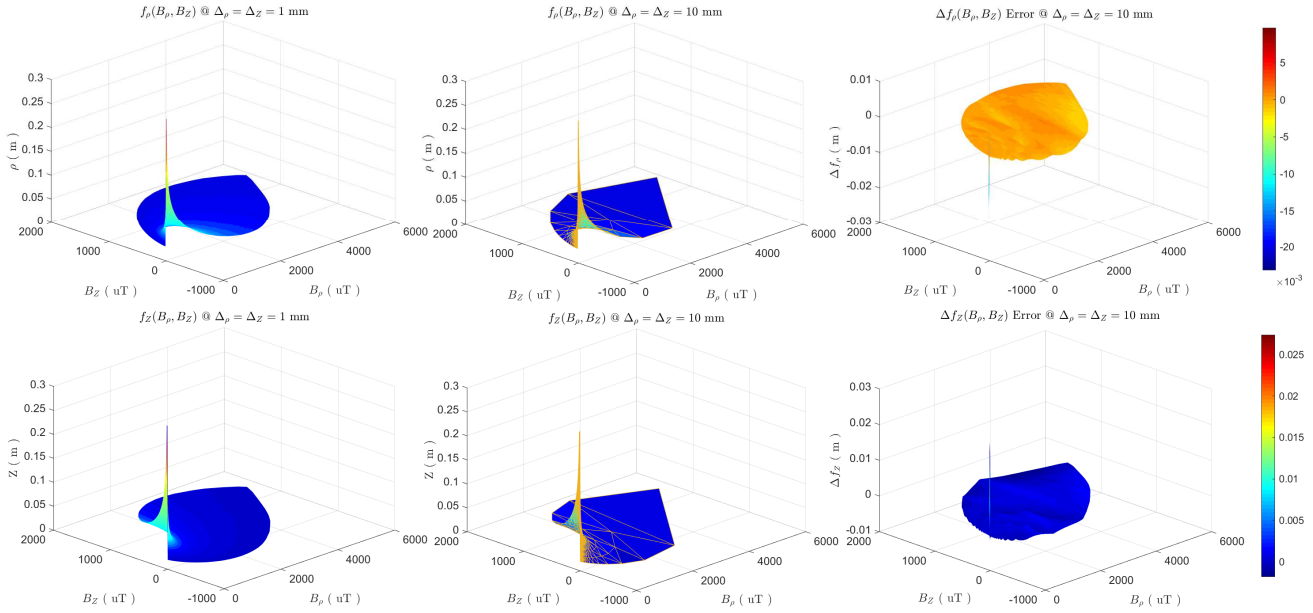

Fig. 6: Scattered interpolation of regression functions $\rho = f_\rho(B_\rho, B_Z)$ and $Z = f_Z(B_\rho, B_Z)$ comparison for different position grids $\Delta\rho = \Delta_Z = 1\,\text{mm}$ and $\Delta\rho = \Delta_Z = 10\,\text{mm}$.

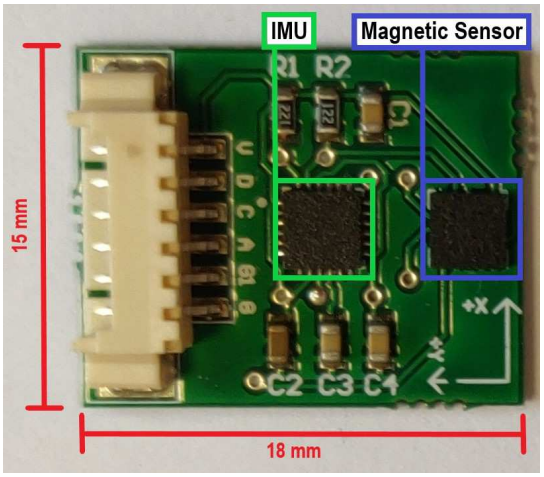

Fig. 7: Wearable sensor prototype. An MPU9250 IMU is used to estimate the sensor couple orientation, while a KMX62-1031 is used as magnetic sensor.

131 $^{\text{LSB}}/_{^\circ/\text{s}}$ and full scale ranges from ± 250 to $2000\,^\circ/\text{s}$ The IMU is mechanically coupled to the high speed digital magnetic sensor KMX62-1031 which has a sample frequency from 0.781 Hz to 1.6 kHz, sensitivity of $0.0366\,^{\mu\text{T}}/_{\text{LSB}}$ and full scale range of $\pm 1200\,\mu\text{T}$. This mechanical coupling allows the system to estimate the magnetic sensor orientation using the IMU data. The use of both external magnetic sensor and IMU may be considered redundant for the marker miniaturization, which is a direct goal for any wearable system. However, this is mandatory due to the sampling rate limitations of the integrated magnetic sensor AK8963 and of known commercially available IMU.

As depicted in Fig. 8a, the sensing module (marked with green letters) comprises the following elements:

A Sensor module with Invensense MPU9250 and Kionix KMX62-1031;
B STM32F446RE MCU on a ST Nucleo-F446RE evaluation board;
C Laptop connected through USB to the MCU, running Matlab as GUI.

The field generator module (marked with blue numbers) comprises the following elements:

1 Aim-TTi EX354TV power supply;
2 Teledyne Lecroy Wavestation 3082 signal generator;
3 ST STEVAL-CCA044V1 power amplifier board;
4 800 turns handcrafted uni-axial bobbin coil with high temperature resistive resin base and 30 AWG magnetic wire, measured impedance of $21\,\Omega$ at 100 Hz.

A 32 V and 1 A power supply is used to feed the field generator module, while the signal generator and the power amplifier were set to generate a sinusoidal wave of 100 Hz and $1\,\text{A}_{peak}$ to the bobbin coil.

The sensing module was set to sample the magnetic flux density with $800\,^{\text{samples}}/_{\text{s}}$, while sampling the acceleration and the angular velocity with $100\,^{\text{samples}}/_{\text{s}}$. The MCU filters and processes the acquired signals, then estimates the sensor couple orientation and the magnetic signal envelope with $100\,^{\text{samples}}/_{\text{s}}$ and finally performs the regressions functions in Eq. (2) using 778 points with 16-bit precision for $\pm 1200\,\mu\text{T}$ for B_ρ and B_Z, and 0 to 30 cm for ρ and Z. To emulate their implementation inside the MCU at the offline test processing stage, the laptop performs the same regression function on Matlab, while for the real-time implementation it is used to show graphically the estimated sensor position and orientation at 100 fps.

Since in this proof-of-concept an IMU sensor in the field generator module is not included, the system axes are determined using the orientation that the tracked sensor has

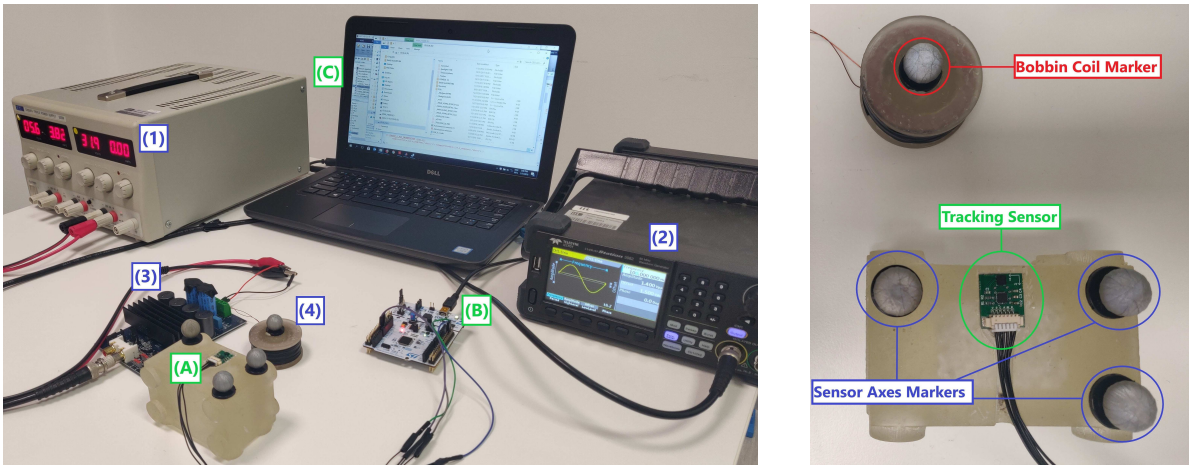

(a) (b)

Fig. 8: Validation system test-up. The field generator module comprises, (1) Power supply, (2) Signal generator, (3) Signal amplifier and (4) Bobbin coil. The receiver module comprises (A) Designed couple sensor, (B) MCU and (C) Laptop running a GUI. Retro-reflective markers are used on the system prototype: one marker is placed in the center of the bobbin coil axis, three are placed aligned with both X and Y sensor axes, and three extra markers are used to fix the VICON® system axes.

for the first ten seconds after initialization. In this section we will present first measurement results using the system uncalibrated. Based on these results we will introduce a calibration algorithm based on a Neural Network (NN) to enhance performance and we will apply this in post-calibration measurement results.

A. Uncalibrated Static and Dynamic Measurements

Both static and dynamical accuracy tests have been performed using a VICON® optical tracking system to obtain the ground truth measurement. VICON® systems provide the necessary accuracy to establish ground through as they operate through retro-reflective markers with an accuracy of $1\,\mathrm{mm}$ with $200\,\mathrm{fps}$. All measurements were performed inside a room of $3\,\mathrm{m}\times4\,\mathrm{m}\times3\,\mathrm{m}$ size with 9 cameras placed $3\,\mathrm{m}$ high. As shown in Fig. 8a four retro-reflective markers were fixed in the proposed system: one was placed in center of the top side of the bobbin coil, three were placed in the sensor holder aligned with the X and Y axes of the sensor, and three extra markers were used to fix the VICON measurement axes. The sensor is positioned $9\,\mathrm{mm}$ below the middle point between the markers that trace the X axis.

The static accuracy test consisted in a comparison of the resulting measurements of both tracking systems of the sensor position with respect to the bobbin coil. For this evaluation we have used 95 different positions inside a half cylinder volume of $20\,\mathrm{cm}$ radius and $13\,\mathrm{cm}$ height, within a maximum measured distance of $21\,\mathrm{cm}$. 5 seconds of data, with the sensor statically positioned in each specific location, were recorded for comparison. As specified in [33], the performance of Madgwick's algorithm in the estimation of the IMU sensor orientation greatly relies on a proportional coefficient of the algorithm loop β, which balances the influence of the gyroscope data (self-referenced dynamic data) over the accelerometer and magnetic sensor data (earth referenced static data). Therefore, we need to consider this to test the sensor orientation accuracy independently, in order to chose the proper β set up for the dynamic accuracy test. The three sensor axes retro-reflective markers movements were recorded along with the IMU sensor data. The sensor holder was then rotated around its three axes once counterclockwise and once clockwise within a range of $\pm90°$ for a rotation duration of 5 s, while the variable magnetic field was generated. The dynamic accuracy test consisted in recording four different types of movements inside a half cylinder volume of $20\,\mathrm{cm}$ radius and $13\,\mathrm{cm}$ height, recorded with both VICON® and prototype system, in particular:

- "T movement" test, where the sensor is moved in parallel to the table plane, first in parallel to the Y axis and then in parallel to the X axis.
- "Circle movement" test, where the sensor is moved in parallel to the table plane following a circular form.
- "Arc movement" test, where the sensor is moved to form arcs traces inside the tracking space.
- "Arbitrary movements" test, where the sensor is moved arbitrarily for 5 seconds inside the tracking space.

Accuracy is evaluated with the spatial root-mean-square error formula revisited as follows,

$$\xi = \sqrt{\frac{1}{n}\sum_{k=1}^{n}((X_k - Xv_k)^2 + (Y_k - Yv_k)^2 + (Z_k - Zv_k)^2)}, \tag{6}$$

where X_k, Y_k and Z_k are the prototype system estimated coordinates, Xv_k, Yv_k, Zv_k are the VICON® estimated coordinates and n is the total test position points for the static test or the recorded number of frames for dynamical tests. The static experimental tests have been performed for two hours while dynamical tests on four hours, for a total experimental time frame of six hours. Fig. 9a shows both the VICON® measured position targets and the system output for each one

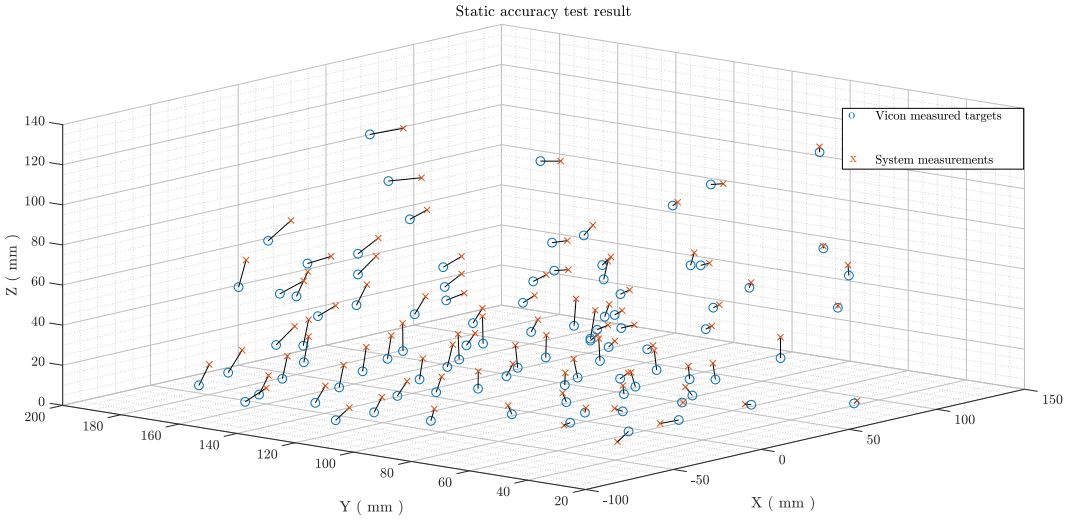

(a)

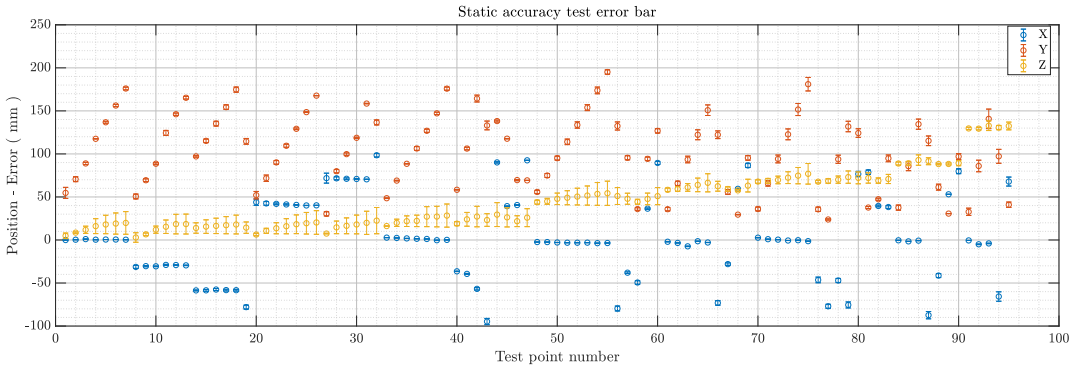

(b)

Fig. 9: Static accuracy experimental test results. VICON® measured targets are marked with blue circles, while system outputs are marked with orange crosses and the distance between them is marked with a black line.

of the trial points, while their deviation is shown by a black line. The resulting spatial accuracy ξ of this test is $7.8\,\mathrm{mm}$. This measurement result is comparable with our previous studies in [28], with the difference of running in 6DOF, which makes it usable in more applications. As shown in Fig. 9b, the mayor contribution to spatial error comes from the Z coordinate. Both X and Y data, which directly depend on ρ, show a growing error as the test point gets further away from the system origin. This is consistent with having used scattered interpolations computed from FEM simulations which do not correspond completely to what is being measured. The sensor orientation RMSE values obtained were $2.15°$, $1.89°$, $1.94°$ and $1.92°$ for β values 0.01, 0.1, 0.3 and 0.5 respectively. Results show that the optimal β value obtained is 0.1 and the minimum orientation RMSE obtained is $1.89°$ which is close to the reported algorithm performance of $1.7°$ RMSE by Madgwick [33]. Dynamical accuracy measurement results are shown in Tab. II. The dynamical measurements are consistent with the static accuracy test result. Fig. 10a, 10b, 10c and 10d show the four best test recording outputs of both VICON® and prototype system. We can observe that the proposed system can only approximately follow the sensor movements. As the sensor gets further away from the system origin results shows a growing position error, more evident in the Z axis in comparison to the XY plane. This supports the previous observation taken from the static accuracy test. To identify the main error source, we used the static accuracy test position points inside the FEM simulation to compute their correspondent simulated magnetic flux density values and compare with the measured magnetic flux values in the form of $\gamma_{ratio\,\rho} = B_{\rho\,sim}/B_{\rho\,meas}$ and $\gamma_{ratio\,Z} = B_{Z\,sim}/B_{Z\,meas}$. As a linear relation between simulated and measured magnetic flux densities is not found (potentially explaining the origin of the difference between simulated and measured magnetic flux density values), we concluded that the scattered interpolation of the regression functions of Eq. (2) needs to be modified to match the measured magnetic flux density values and enhance system performance.

B. Calibration Procedure

In order to obtain the regression functions with data that properly represents the generated magnetic field, two approaches are possible, in particular:

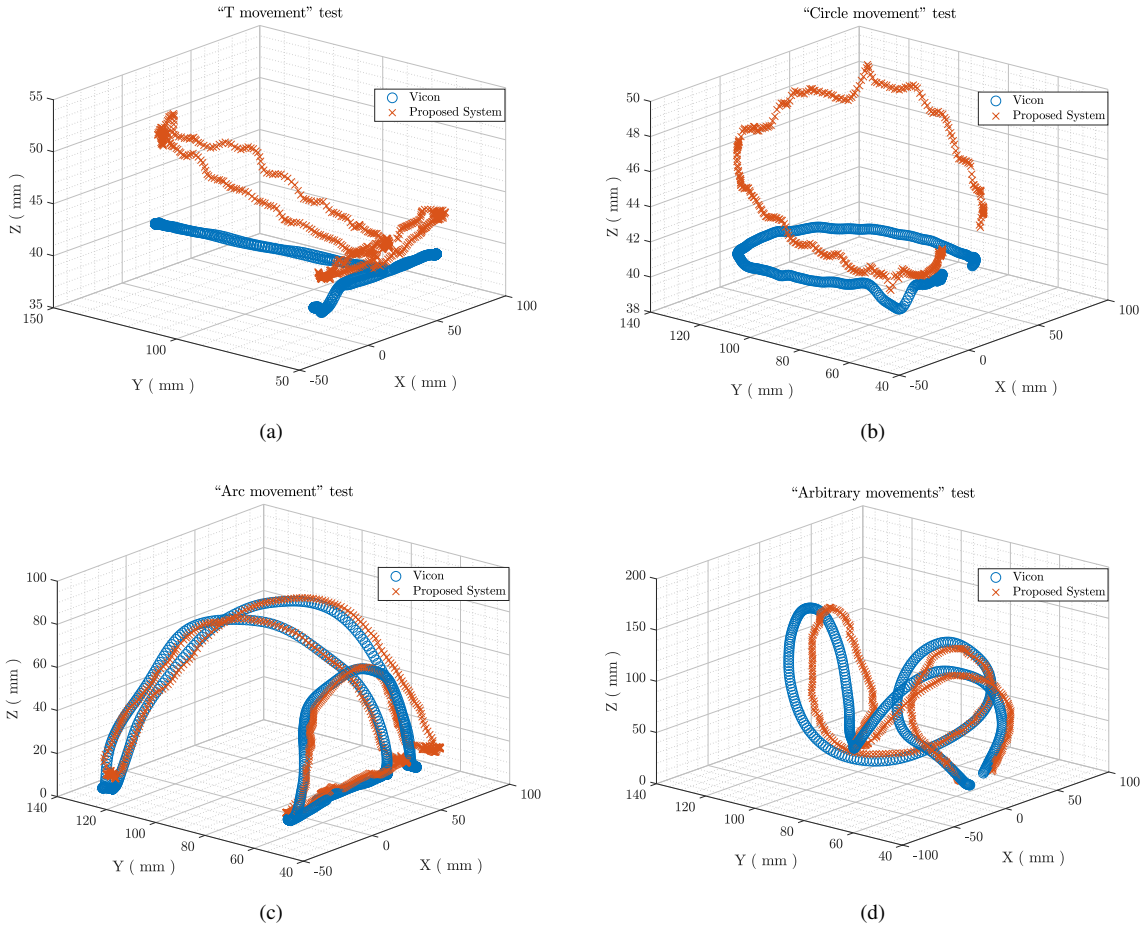

Fig. 10: Dynamic accuracy experimental test results. "T movement" best test performance (a). "Circle movement" best test performance (b). "Arc movement" best test performance (c). "Arbitrary movements" best test performance (d).

TABLE II: Dynamic Accuracy Measurements

Movement Type	T				Circle			Arc			Arbitrary		
Test Number	#1	#2	#3	#4	#1	#2	#3	#1	#2	#3	#1	#2	#3
ξ (mm)	6.4	6.9	6.2	5.3	8	7.1	6.7	7.5	8.9	10.4	7.5	9.4	7.9
ξ avg (mm)	7.6												

1 *Entirely reconstruct the regression functions by substituting the simulated data sets with measured magnetic flux density on each position point of the desired grid.*
This approach has the drawback of being unpractical because it requires the correct positioning of the sensor in each of a large data set of positions points.

2 *Use a representative number measurements in order to form a data set of position points and magnetic flux density measurements in our tracking space of interest. Compute FEM simulations of the magnetic flux density on each position point of the data set. Then find a regression relationship between the FEM simulation results and the measurements obtained on the same position points and finally enable a generalizable fitting that uses as input the FEM simulation results and as target the measurements taken.*
This approach has the advantage of adapting (calibrating) the large simulated data set of the previous regression functions using a smaller data set of the measured magnetic flux density.

We followed the second approach because of its inherent viability and thus, the possibility of re-using the large data set obtained in FEM simulation. Using thirty-nine of the ninety-five static test measurement, a data set directly related to the generated magnetic field is formed covering test positions points in the ranges $47\,\mathrm{mm} \leq \rho \leq 160\,\mathrm{mm}$ and $8\,\mathrm{mm} \leq Z \leq 130\,\mathrm{mm}$. The relationship between simulated and measured magnetic flux density data sets, defined by the ratios $\gamma_{ratio\,\rho}$ and $\gamma_{ratio\,Z}$, followed a non-linear trend. Moreover, there were not any identifiable mathematical relations that could be used for simple regression fitting techniques. Hence, we have chosen to train a two-layer feed-forward two-inputs two-outputs and sixteen neuron Neural Network (NN). The NN uses as input the simulated magnetic flux density values computed on a known set of position points, formed from a third of the static accuracy test position points.

The magnetic flux density measured on the same set of position points are used as targets. A Bayesian Regularization algorithm was implemented with 70% of samples used for training and 30% used for testing. Finally, the trained NN is fed with the uncalibrated regression functions magnetic flux density data set, generating a new data set to form the calibrated regression functions. These regression functions are now optimized to work with the magnetic field measured during the static accuracy test.

C. Post-calibration Measurements

Using the previously recorded test data with the calibrated regression functions of Eq. (2), new static and dynamic accuracy test results were obtained. Fig. 11a shows the post-calibration static accuracy test results. In comparison to the previous results shown in Fig. 9 we observe that the responses are closer to the target points in the covered tracking space. The system accuracy was measured using Eq. (6), resulting in an spatial RMSE $\xi = 2.6\,\mathrm{mm}$. This represents a relative error of $1.23\,\%$ the maximum tracked distance $(21\,\mathrm{cm})$ and proves that the system performance improved with the executed calibration procedure. Compared to the pre-calibration relative error of $3.71\,\%$, indeed, accuracy gain is $200\,\%$. Supporting the above observation, Fig. 11b shows the system accuracy enhancements both on the Z axis and on the XY plane for the test point positioned farthest from the system origin, compared to Fig. 9b. System performance enhancement is also highlighted in Tab. III which shows the results of each dynamical test as well as their average accuracy, highlighting a $40.7\,\%$ accuracy gain from the pre-calibration test result. The improvement on the Z estimation is more evident on Figs. 12a and 12b compared to Figs. 10a and 10b. While the "arcs movement" test of Fig. 12c show only a slight improvement both numerically and graphically compared to 10c, the "arbitrary movements" show a more evident improvement after calibration. As shown in Fig. 12d the proposed system can follow properly very complex traces.

D. Wireless Communication Capabilities

In order to test the feasibility of replacing USB data transmission with wireless communication, we have added an ST X-NUCLEO-IDB05A1 expansion board on top of our ST Nucleo-F446RE board. This board interfaces the STM32F446RE MCU with a SPBTLE-RF network processor module that includes an embedded BLE protocol stack, enabling BLE v4.2 compliant communication for the sensing module of our prototype. We defined a custom service with seven characteristics, X, Y, Z, q_{R0}, q_{R1}, q_{R2} and q_{R3}, through which we were able to broadcast the sensor position and relative quaternion with $100\,{}^{\mathrm{samples}}/_{\mathrm{s}}$ rate, 16-bit and 32-bit precision respectively. We received and verified the transmitted data correctness through a smartphone using a BLE Analyser application, demonstrating the wireless communication capabilities of our system. The overall measured current consumption during transmission was $51.1\,\mathrm{mA}$.

VI. Discussion

We introduce a figure of merit (FOM) Γ to compactly collocate the designed tracking system performance and wearability in comparison to state-of-the art devices either commercially available and research developed. The FOM focuses on both system accuracy and range, but at the same time highlights the system wearability (and complexity) which is the main characteristic in which both the proposed system algorithm and hardware architecture focuses. The FOM is defined as,

$$\Gamma = \frac{\xi_P}{R_M}\,\frac{V_M}{DOF}. \tag{7}$$

The first term of Γ includes the position static accuracy ξ_P of the tracking device, since this is the main performance indicator. Considering that the performance of magnetic tracking decays with the sensor to field generator distance, Γ is proportional to static accuracy ξ_P over the tracking range R_M ratio. The second term accounts for the device markers wearability and usage flexibility. This comprises the marker volume V_M (in the nominator), as with a higher sensor volume the system becomes less useful for wearable applications. To unify the evaluation criteria among the reported magnetic tracking systems, we take into account only the tracked marker volume, as it is supposed to be worn in parts of the body that significantly move. We therefore ignore the volume of processing units or data transmitters that do not impact in the moving object tracking. Finally, the second term denominator comprises the number of DOF to indicate a Γ improvement as DOF increases. Tab. IV compares the state-of-the-art systems with our prototype in terms of position static accuracy (mm), orientation accuracy $(^\circ)$, tracking range (cm), output update rate $({}^{\mathrm{samples}}/_{\mathrm{s}})$, degrees of freedom, the capability of wireless communication between tracking markers or wearable processing unit and the end-user device, and Γ. We observe that by using the FOM Γ as an indicator, our system is ranked only fourth in a list of devices composed by several commercial and research developed system. This can be considered a very good result for such a low complexity and non optimized prototype made with off-the-shelf components. Moreover, compared to wireless only systems the prototype ranks only second w.r.t the magnetic tracking system gold standard Polhemus G4 [18] that uses deeply engineered micro-sensors. Observe also that on Tab. IV most of the compared system algorithms are run on a CPU or a GPU: Polhemus G4 transmits the sensed data wirelessly to the user CPU and process all data in the end-user device. In our system, the algorithm runs directly on the sensor module, particularly on a Cortex-M4 as we focus on the wearability and portability of the solution regardless of the end-user device performance. Observe that our current prototype includes a BLE v4.2 compliant communication module. However, futher optimizations are possible and need to be considered in further studies, in particular on a battery life-latency trade-off basis. A minimum latency of $676.7\,\mu\mathrm{s}$ for an error-free one-way ATT exchange transmission was reported in [41] considering the minimum connection interval of $7.5\,\mathrm{ms}$. Since two ATT exchanges are necessary for the notification of a single sensor 22 bytes payload, we can expect a minimum notification delay of $1.35\,\mathrm{ms}$. We consider this

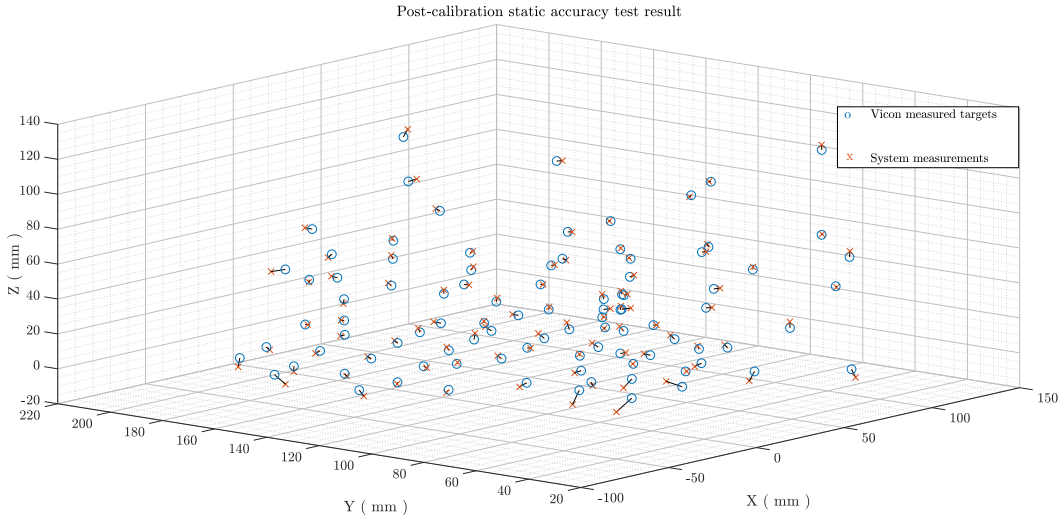

(a)

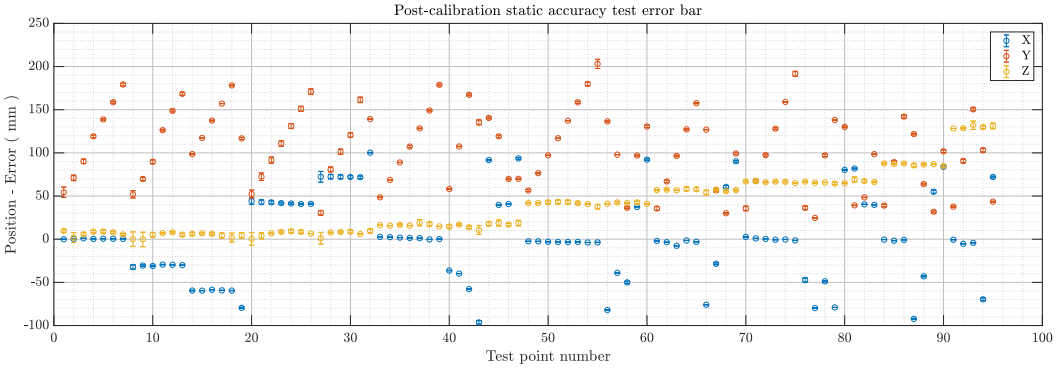

(b)

Fig. 11: Post-calibration static accuracy experimental test results. Referenced targets are marked with red circles, while system outputs are marked with red crosses and the distance between them is marked with a black line.

TABLE III: Dynamic Accuracy Measurements

Movement Type	T				Circle			Arc			Arbitrary		
Test Number	#1	#2	#3	#4	#1	#2	#3	#1	#2	#3	#1	#2	#3
ξ (mm)	3	3.9	3.6	2.7	5.7	3.4	4.7	7.4	8.4	10.4	5.1	6.4	5.4
ξ avg (mm)	5.4												
Pre-calibration ξ avg (mm)	7.6												
Calibration ξ Gain (%)	40.7												

result as a starting point for multi-sensing and system upgrade and optimization, for example regarding the use of a BLE v5 module. For instance, we can consider two scenarios, one where the regressions functions are running on the sensing module MCU and other where these are running on the GUI. In both scenarios the data to be transmitted (using for instance a custom characteristic) for each sensor comprises three 16-bit words (either for the three sensor coordinates or the three sensor axes magnetic measurement amplitude) plus four 32-bit words for the sensor orientation quaternion. Observe that [42] exposes a maximum data throughput for BLE v4.2 of $236.7\,\mathrm{kbps}$ which would allow us to transmit a maximum payload of 13 sensors, given a $100\,{}^{\mathrm{samples}}/_{\mathrm{s}}$ sensor update rate. On the other hand, [43] reports maximum data throughput for BLE v5 between $1.3\,\mathrm{Mbps}$ and $800\,\mathrm{kbps}$ using notifications. These data rates capabilities would allow our system to transmit at least a payload for a maximum of 45 sensors. Therefore, our solution remains a very good candidate to enable precise tracking of a considerable number of nodes simultaneously, as in finger tracking applications. We can conclude that there is still space for improvement by further enhancing calibration in order to enhance the system tracking accuracy. Another viable option would be to use magnetic sensors with a higher resolution, while maintaining the low volume of the sensing module and a sampling rate equal or higher than the current sensor sampling rate. Another interesting aspect regards the orientation accuracy of those devices that have 6DOF. Our prototype is worse than commercial devices while

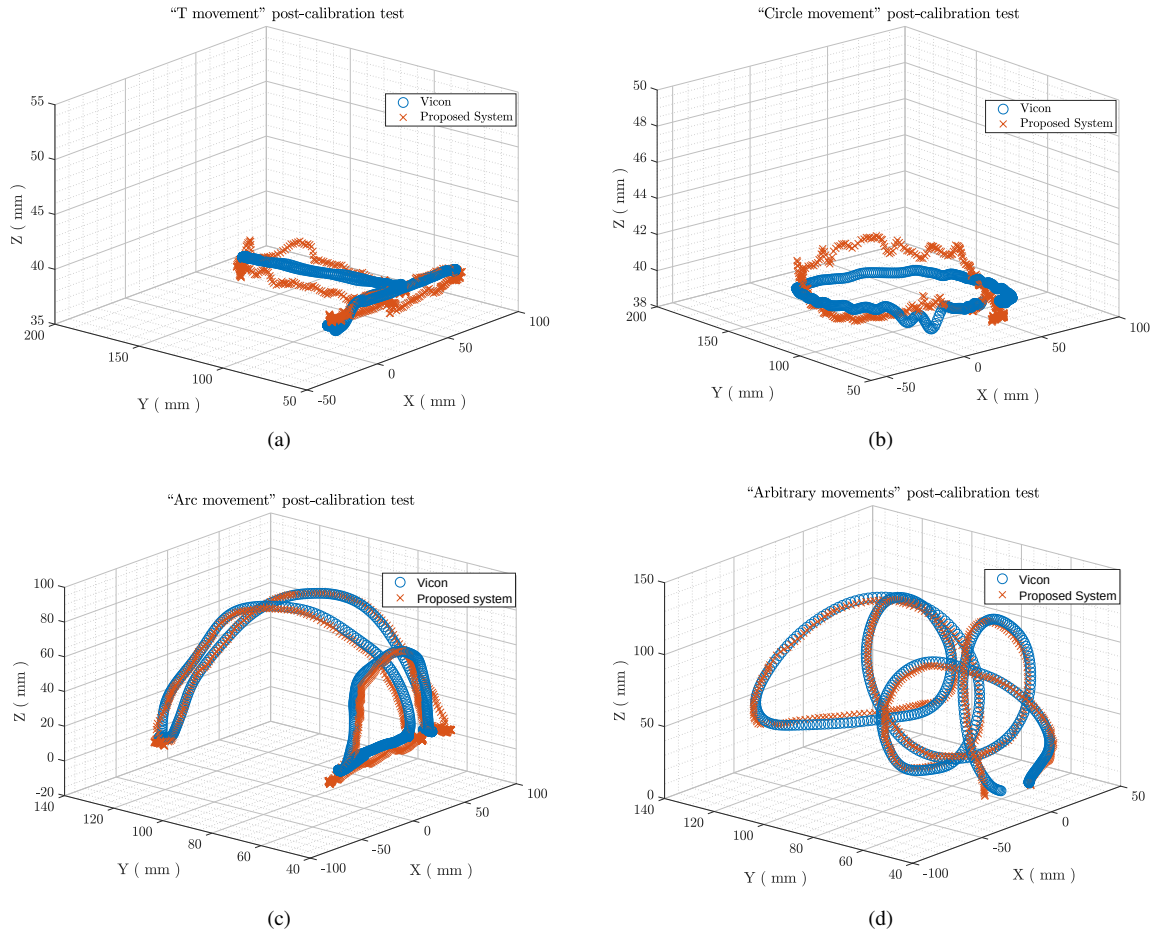

Fig. 12: Post-calibration dynamic accuracy test results. "T movement" best test performance (a). "Circle movement" best test performance (b). "Arc movement" best test performance (c). "Arbitrary movements" best test performance (d).

TABLE IV: Magnetic Tracking Systems state-of-the-art Comparison.

System	Processor	Position Accuracy (mm)	Range (cm)	Update Rate ($^{samples}/_{s}$)	Wireless Feature	DOF	Orientation Accuracy (°)	Marker Volume (mm^3)	Γ (mm^3)
Patriot [20]	NA^+	1.524	91.44	60	No	6	0.4	$28.3 \times 22.9 \times 15.2$	2.74
Aurora [38]	NA^+	0.88 - 1.4	50 - 66	40	No	6	0.48 - 0.55	$19.8 \times 7.9 \times 7.9$	0.36 - 0.44
TrakSTAR [39]	NA^+	1.4	66	20 - 255	No	6	0.5	$19.8 \times 7.9 \times 7.9$	0.44
Finexus [21]	CPU	1.33	12	320	No	3	-	$10 \times \pi \times 5^2$	2.9
Fernandez [28]	CPU	6.5	24	66	No	5	-	$42 \times 30 \times 3$	20.47
G4 [18]	CPU	2 - 12.7	100 - 300	120	Yes	6	0.5 - 1	$22.9 \times 28.2 \times 15.2$	3.27 - 20.78
G4 [18] micro-sensor	CPU	10.16	150	120	Yes	6	0.5	$10 \times \pi \times 0.9^2$	0.029
Patriot Wireless [19]	NA^+	7.5	76.2	50	Yes	6	1	$88.9 \times 42.2 \times 24.6$	151.39
IM6D [22]	GPU	1 - 5	20	30	Yes	6	1.89 - 2.21	4000	3.34 -16.67
TRing [27]	CPU	8.6	12	30	Yes	6	6	$35 \times 22 \times 25$	229.9
GaussSense [40]	CPU	0.42	10	60	Yes	5	-	$30 \times \pi \times 4^2$	1.27
This work	Cortex-M4	**2.6**	**21**	**100**	**Yes***	6	**1.89**	$\mathbf{18 \times 15 \times 2}$	**1.11**

* = The prototype currently does not include a wireless transceiver, but it is conceived to specifically support it.
NA^+ = Unknown embedded system.
- = Not reported.

maintaining comparable performance w.r.t the IM6D system [22]. However, even if the difference compared to commercial devices is not large, the orientation accuracy of our prototype was measured under dynamical conditions, while commercial devices performance regards static conditions, i.e., the typical optimization target of tracking systems. We can estimate the power consumption of a final prototype including wireless connectivity as a way to understand feasibility of a full functioning wearable device. As the measured MCU average current consumption is $42.4\,\mathrm{mA}$ during sensor position estimation through USB, while power is $51.1\,\mathrm{mA}$ with BLE v4.2 broadcasting. We could also use the current consumption of a BLE v5 BGM13 module under transmitting conditions, which is $8.5\,\mathrm{mA}$. Current consumption estimation increases for multiple sensors up to $4.1\,\mathrm{mA}$ for each extra sensor couple. Therefore, a final device including six pairs of sensors, a BLE v5 module and a $2000\,\mathrm{mA\,h}$ accumulator would have an estimated battery life of $27\,\mathrm{h}$. Such final system would be perfectly tailored for applications such as hand fingers tracking for neuroscience studies, surgical instrumentation guiding for medical training. As mentioned in Sec. V, the dynamical tests were performed in a time frame of four hours and we can consider this as our maximum system validation time to sustain the reported performance. Next works will deal with investigations on system performance-level variability after a calibration procedure.

VII. Conclusion

A 6DOF magnetic tracking system based on IMU-based orientation estimation of the sensor and scattered interpolation as regression functions has been presented. The system simplifies the position tracking algorithm, therefore enabling the potential tracking of several sensors using a single MCU, and allowing the development of a multi-sensor, wearable and wireless device. Future works can include the optimization of wireless communication, and the improvement of system tracking accuracy and working range. These last aspect can be achieved either by changing the magnetic flux density sensor and optimizing further the calibration procedure. Final optimizations will deal with the implementation of an online calibration procedure to ensure an accuracy performance for long-term applications. Such procedure can regard zero-bias calibration of the IMU and magnetic sensors when required and monitor the magnetic field degradation due to long-term usage. This could be achieved by using a fixed sensor with a known referenced position w.r.t the magnetic field generator, through which the system periodically monitors how the magnetic field changes over time. Finally, multiple sensors tracking can be considered using a single MCU.

Acknowledgment

The authors would like to thank PhD. Maria Carla Memeo, Congition Motion and Neuroscience research Line – Istituto Italiano di Tecnologia, for her precious support on VICON measurements, and M. Sc. Cecilia Bosia, Dipartimento di Elettronica e Telecomunicazioni – Politecnico di Torino, for her valuable contribution to the system algorithm development.

References

[1] VICON, "Motion Capture for Entertainment," https://www.vicon.com/motion-capture/entertainment, 2019.

[2] M. Groeger, K. Arbter, and G. Hirzinger, "Motion Tracking for Minimally Invasive Robotic Surgery," in *Medical Robotics*, 2008.

[3] C. Ansuini, A. Cavallo, C. Bertone, and C. Becchio, "The visible face of intention: why kinematics matters," *Frontiers in Psychology*, vol. 5, p. 815, 2014.

[4] E. van der Kruk and M. M. Reijne, "Accuracy of human motion capture systems for sport applications; state-of-the-art review," *European Journal of Sport Science*, vol. 18, no. 6, pp. 806–819, 2018.

[5] T. Dutta, "Evaluation of the Kinect sensor for 3-D kinematic measurement in the workplace," *Applied Ergonomics*, vol. 43, no. 4, pp. 645–649, 2012.

[6] A. M. Franz, T. Haidegger, W. Birkfellner, K. Cleary, T. M. Peters, and L. Maier-Hein, "Electromagnetic Tracking in Medicine - A Review of Technology, Validation, and Applications," *IEEE transactions on medical imaging*, vol. 33, no. 8, pp. 1702–1725, 2014.

[7] E. Bonizzoni, A. Puiatti, S. Sapienza, P. M. Ros, D. Demarchi, and P. Bonato, "UWB Tracking for Home Care Systems with Off-the-Shelf Components," in *IEEE International Symposium on Circuits and Systems (ISCAS)*, 2018, pp. 1–5.

[8] S. Zihajehzadeh, P. K. Yoon, B.-S. Kang, and E. J. Park, "UWB-aided inertial motion capture for lower body 3-D dynamic activity and trajectory tracking," *IEEE Transactions on Instrumentation and Measurement*, vol. 64, no. 12, pp. 3577–3587, 2015.

[9] C. Li, L. Mo, and D. Zhang, "Review on UHF RFID Localization methods," *IEEE Journal of Radio Frequency Identification*, 2019.

[10] A.-C. Petre, C. Chilipirea, M. Baratchi, C. Dobre, and M. van Steen, "WiFi tracking of pedestrian behavior," in *Smart Sensors Networks*, 2017, pp. 309–337.

[11] SiLabs, "Bluetooth Direction Finding: Angle of Arrival (AoA) and Angle of Departure (AoD)," https://www.silabs.com/products/wireless/learning-center/bluetooth/bluetooth-direction-finding, 2019.

[12] S. Lehtimaki, "Understanding advanced bluetooth angle estimation techniques for real-time locationing," *Embedded World*, 2018.

[13] VICON, "VICON Camera Systems," https://www.vicon.com/products/, 2019.

[14] NDI, "NDI Products," https://www.ndigital.com/products/, 2019.

[15] Leap Motion, "Technology," https://www.leapmotion.com/en/technology, 2019.

[16] J. Guna, G. Jakus, M. Pogačnik, S. Tomažič, and J. Sodnik, "An Analysis of the Precision and Reliability of the Leap Motion Sensor and Its Suitability for Static and Dynamic Tracking," *Sensors*, vol. 14, no. 2, pp. 3702–3720, 2014.

[17] A. S. Mathur, "Low cost virtual reality for medical training," in *IEEE Virtual Reality (VR)*, 2015, pp. 345–346.

[18] Polhemus, "Polhemus G4," https://polhemus.com/motion-tracking/all-trackers/g4#collapseFour, 2019.

[19] ——, "Polhemus patriot wireless," https://polhemus.com/motion-tracking/all-trackers/patriot-wireless, 2019.

[20] ——, "Polhemus patriot," https://polhemus.com/motion-tracking/all-trackers/patriot/, 2019.

[21] K.-Y. Chen, S. N. Patel, and S. Keller, "Finexus: Tracking Precise Motions of Multiple Fingertips Using Magnetic Sensing," in *Proceedings of the 2016 CHI Conference on Human Factors in Computing Systems*, 2016, pp. 1504–1514.

[22] J. Huang, T. Mori, K. Takashima, S. Hashi, and Y. Kitamura, "IM6D: Magnetic Tracking System with 6-DOF Passive Markers for Dexterous 3D Interaction and Motion," *ACM Transactions on Graphics (TOG)*, vol. 34, no. 6, p. 217, 2015.

[23] J. Klein, C. Peters, J. Martín, M. Laurenzis, and M. B. Hullin, "Tracking objects outside the line of sight using 2D intensity images," *Scientific Reports*, vol. 6, p. 32491, 2016.

[24] M. Memeo and L. Brayda, "Mind the Bump: Effect of Geometrical Descriptors on the Perception of Curved Surfaces with a Novel Tactile Mouse," in *International Conference on Human Haptic Sensing and Touch Enabled Computer Applications*, 2016, pp. 438–448.

[25] M. Memeo, V. A. de Jesus Oliveira, L. Nedel, A. Maciel, and L. Brayda, "Tactile treasure map: Integrating allocentric and egocentric information for tactile guidance," in *International AsiaHaptics conference*, 2016, pp. 369–374.

[26] M. Memeo and L. Brayda, "How geometrical descriptors help to build cognitive maps of solid geometry with a 3DOF tactile mouse," in *International Conference on Human Haptic Sensing and Touch Enabled Computer Applications*, 2016, pp. 75–85.

[27] S. H. Yoon, Y. Zhang, K. Huo, and K. Ramani, "TRing: Instant and Customizable Interactions with Objects Using an Embedded Magnet and a Finger-Worn Device," in *Proceedings of the 29th Annual Symposium on User Interface Software and Technology*, 2016, pp. 169–181.

[28] D. A. Fernandez G, E. Macrelli, D. Demarchi, and M. Crepaldi, "High-Accuracy Wireless 6DOF Magnetic Tracking System Based on FEM Modeling," in *IEEE International Conference on Electronics, Circuits and Systems (ICECS)*, 2018, pp. 413–416.

[29] T. L. Chow, *Introduction to Electromagnetic Theory: A Modern Perspective*. Jones & Bartlett Learning, 2006.

[30] F. H. Raab, E. B. Blood, T. O. Steiner, and H. R. Jones, "Magnetic Position and Orientation Tracking System," *IEEE Transactions on Aerospace and Electronic Systems*, no. 5, pp. 709–718, 1979.

[31] E. E. Callaghan and S. H. Maslen, "The Magnetic Field of a Finite Solenoid," 1960.

[32] F. Attivissimo, A. M. L. Lanzolla, S. Carlone, P. Larizza, and G. Brunetti, "A novel electromagnetic tracking system for surgery navigation," *Computer Assisted Surgery*, vol. 23, no. 1, pp. 42–52, 2018.

[33] S. O. Madgwick, A. J. Harrison, and R. Vaidyanathan, "Estimation of IMU and MARG Orientation Using a Gradient Descent Algorithm," in *IEEE International Conference on Rehabilitation Robotics (ICORR)*, 2011, pp. 1–7.

[34] X. Li and Y. Wang, "Evaluation of ahrs algorithms for foot-mounted inertial-based indoor navigation systems," *Open Geosciences*, vol. 11, no. 1, pp. 48–63, 2019.

[35] X. Li, Y. Wang, and K. Khoshelham, "Uwb/pdr tightly coupled navigation with robust extended kalman filter for nlos environments," *Mobile Information Systems*, vol. 2018, 2018.

[36] A. Cavallo, A. Cirillo, P. Cirillo, G. De Maria, P. Falco, C. Natale, and S. Pirozzi, "Experimental comparison of sensor fusion algorithms for attitude estimation," *IFAC Proceedings Volumes*, vol. 47, no. 3, pp. 7585–7591, 2014.

[37] I. Amidror, "Scattered data interpolation methods for electronic imaging systems: a survey," *Journal of Electronic Imaging*, vol. 11, no. 2, pp. 157–177, 2002.

[38] NDI, "NDI Aurora," https://www.ndigital.com/medical/products/aurora/, 2019.

[39] ——, "NDI driveBAY and trackSTAR," https://www.ndigital.com/msci/products/drivebay-trakstar/, 2019.

[40] R.-H. Liang, K.-Y. Cheng, C.-H. Su, C.-T. Weng, B.-Y. Chen, and D.-N. Yang, "GaussSense: attachable stylus sensing using magnetic sensor grid," in *Proceedings of the 25th annual ACM symposium on User interface software and technology*, 2012, pp. 319–326.

[41] C. Gomez, J. Oller, and J. Paradells, "Overview and evaluation of bluetooth low energy: An emerging low-power wireless technology," *Sensors*, vol. 12, no. 9, pp. 11 734–11 753, 2012.

[42] J. Tosi, F. Taffoni, M. Santacatterina, R. Sannino, and D. Formica, "Performance evaluation of Bluetooth low energy: a systematic review," *Sensors*, vol. 17, no. 12, p. 2898, 2017.

[43] P. Bulić, G. Kojek, and A. Biasizzo, "Data transmission efficiency in Bluetooth Low Energy versions," *Sensors*, vol. 19, no. 17, p. 3746, 2019.

David A. Fernandez G. obtained his M.S. degree at Electronic Engineering from the Politecnico di Torino and his Bachelor's degree at Electrical Engineering from the Universidad Central de Venezuela (UCV), both at 2016 due to a Double Degree's program won by student merits. During 2016 worked inside MiNES (Micro&Nano Electronic Systems, http://mines.polito.it) Laboratory of Politecnico di Torino. He is now a Ph.D. student from the Politecnico di Torino (PoliTo) working alongside the MiNES Laboratory and the Electronic Design Laboratory (EDL) facility at the Istituto Italiano di Tecnologia for Human Technology in Genova. His main activities involves the design and development, both of hardware and software, of a high accuracy 6DOF tracking system for small volumes, which final applications can go from commercial wearable devices to surgical guidance systems.

Paolo Motto Ros is Senior Post-Doc Researcher at Politecnico di Torino (Torino, Italy), Dipartimento di Elettronica e Telecomunicazioni, with the MiNES (Micro&Nano Electronic Systems) group. He received the electronic engineering degree and the Ph.D. in electronic engineering from the Politecnico di Torino, Torino, Italy, in 2005 and 2009, respectively. From 2009 to 2012 he was with Neuronica Laboratory (Dipartimento di Elettronica, Politecnico di Torino) as post-doc researcher, working on assistive technologies, computer vision and learning machines projects (jointly with, 2006-2011, Istituto Nazionale Fisica Nucleare, INFN, Italy). From 2012 to 2019 he was with Istituto Italiano di Tecnologia (Center for Space Human Robotics, CSHR, Torino, Italy, and, since 2016, Electronic Design Laboratory, EDL, Genova, Italy) as senior (since 2014) post-doc researcher, working on bio-inspired electronics for biomedical and humanoid robotic applications. He joined the Politecnico di Torino, Dipartimento di Elettronica e Telecomunicazioni, in 2019. IEEE member since 2016, and member of the Circuits And Systems (CAS) society; organizing staff member of the IEEE BioCAS 2017 conference, and organizing committee member of the IEEE ICECS 2019 conference. He counts more than 40 publications; current research interests include: event-driven digital integrated circuits, architectures, and systems; low-power smart sensor networks; bio-inspired electronics; biomedical and humanoid robotic applications.

Danilo Demarchi (M10-SM13) received Engineering Degree and Ph.D. in Electronics Engineering from Politecnico di Torino, Italy, in 1991 and 1995, respectively. Full position as Associate Professor at Politecnico di Torino, Department of Electronics and Telecommunications. Visiting Professor at EPFL Lausanne and at Tel Aviv University. Visiting Scientist (August 2018) at MIT and Harvard Medical School. Author and co-author of 3 patents and more than 200 scientific publications in international journals and peer-reviewed conference proceedings. Leading the MiNES (Micro&Nano Electronic Systems, http://mines.polito.it) Laboratory of Politecnico di Torino. Member of the BioCAS Technical Committee, Associate Editor of the Transactions on Biomedical Circuits and Systems (TBioCAS), Associate Editor of IEEE Sensors and of the Springer Journal BioNanoScience. General Chair of BioCAS (Biomedical Circuits and Systems) Conference edition in Torino, October 2017 and founder of IEEE FoodCAS Workshop (Circuits and Systems for the Food Chain).

Marco Crepaldi received the engineering degree (summa cum laude) and the Ph.D. in electronic engineering from the Politecnico di Torino (Polito), Turin, Italy, in 2005 and 2009, respectively. During 2008 he was a Visiting Scholar at the Electrical Engineering Department of Columbia University in the City of New York. After the Ph.D., he worked as a Postdoc at the VLSI-Lab, Electrical Engineering department, PoliTo, and then as a Postdoc at the former Istituto Italiano di Tecnologia@PoliTo Center for Space Human Robotics (IIT-CSHR). He is now the coordinator of the Electronics Design Lab (edl.iit.it) at the IIT Center for Human Technology in Genova. His scientific activity is related to the analysis, simulation and development of integrated event-driven and all-digital Impulse-Radio Ultra-Wide Band (IR-UWB) systems. He is author and co-author of more than 60 publications and two international patents. He is an IEEE member since 2009.